Topological Radiated Dendrites Featuring Persistent Bactericidal Activity for Daily Personal Protection

Zhiheng Li, Jie Wang, Ruichen Shen, Na Chen, Xinyuan Qin, Wenjie Wang, and Quan Yuan*

Many substances in nature show radiated topological structure and possess excellent bio-adhesion ability. Herein, regulating the topological structure of Zn_2GeO_4:Mn persistent phosphors is achieved with a molecular coordination method. The morphology of the Zn_2GeO_4:Mn phosphors is well-tuned from nanorods to radiated dendrites by changing the coordination capability of the surface ligand. Due to the structural matching and multivalent interactions, Zn_2GeO_4:Mn radiated dendrites show strong adhesion affinity toward organisms. Moreover, the porous radiated structure offers Zn_2GeO_4:Mn with a large surface area for photocatalysis. Efficient bacterial adhesion and good long persistent photocatalysis activity are observed in the Zn_2GeO_4:Mn radiated dendrites, which endows Zn_2GeO_4:Mn with persistent antibacterial activity even in the dark. Further, the Zn_2GeO_4:Mn spike flowers loaded fabrics exhibit potent persistent antibacterial properties. Mask and towel fabricated with the antibacterial fabrics can inhibit bacterial growth effectively and no bacteria are observed to pass through the antibacterial mask, suggesting that antibacterial mask can guarantee our health and can be utilized repeatedly. The developed Zn_2GeO_4:Mn dendrites possess ideal ability in long-term bacterial inhibition, making them valuable in the fields of medical protection and food packaging.

1. Introduction

The nature system has evolved many substances with radiated topological structures ranging from microcosmic viruses to macroscopic pollen grains.[1] These radiated substances show strong adhesion ability and can bind to many kinds of organisms through structural matching and multivalent

interactions.[2] For instance, viruses show rough topologies due to the spiky proteins on their surface, and these proteins can enhance the binding strength between viruses and the host cell by forming multivalent interactions.[3] Plant pollen grains can easily adhere to the legs of bees and other insects with their surface sharp raised structures for pollen spreading and pollination.[1e] In deed, functional materials with radiated topological structure possess abundant surface active sites and can achieve high-affinity recognition for applications ranging from catalysis to immunotherapy.[4] Studies reported that $SiC@MoS_2$ nanoparticles with radiated morphology displayed excellent photocatalytic behavior due to their large exposed surface active sites.[4a] Further, TiO_2 spiky microparticles can activate immune response through their multivalent interaction with the cell membrane.[1c] These studies show that the properties and functions of materials are strongly dependent upon their morphologies. Developing functional materials with controllable topological structure can deepen our understanding on the structure-performance relationships of these materials and provide valuable tools for fields including biomedicine and energy.

Topological structure refers to the surface structure with roughness, pore, or certain orientation.[5] Topological structure introduces abundant active sites and spatial orientation to the binding between topological materials and organisms, leading to the formation of multivalent interactions. The multivalent interactions can enhance the binding affinity of materials to organisms and promote their exchange of matter or energy.[6] Principally, the topological structure of materials is derived from the different growth rates of crystallographic facets.[7] During the growth of the materials, ligands in the reaction system can inhibit the growth of crystallographic facets by coordinative binding with the surface exposed metal ions, leading to the generation of crystals with certain topological structure.[8] Therefore, ligand-based molecular coordination strategy is a promising method for regulating the topological structure of functional materials.

Here, we reported a molecular coordination method to regulate the topological structure of persistent phosphors. Specifically, by changing the coordination ability of the organic amine in the

Z. H. Li, Dr. J. Wang, N. Chen, X. Y. Qin, Prof. Q. Yuan
Key Laboratory of Biomedical Polymers of Ministry of Education
College of Chemistry and Molecular Sciences
School of Microelectronics
Wuhan University
Wuhan 430072, China
E-mail: yuanquan@whu.edu.cn
R. C. Shen, W. J. Wang, Prof. Q. Yuan
Institute of Chemical Biology and Nanomedicine
State Key Laboratory of Chemo/Biosensing and Chemometrics
College of Chemistry and Chemical Engineering
Hunan University
Changsha 410082, China

The ORCID identification number(s) for the author(s) of this article can be found under https://doi.org/10.1002/smll.202100562.

reaction system, the topological structure of Zn_2GeO_4:Mn persistent phosphors can be well-tuned from nanorods to flower-like radiated dendrites. The Zn_2GeO_4:Mn radiated dendrites show strong adhesion affinity toward bacteria. Moreover, owing to their long persistent photocatalysis (LPPC) function,[9] Zn_2GeO_4:Mn can efficiently produce reactive oxygen species (ROS) to inhibit bacterial growth even in the dark. The Zn_2GeO_4:Mn radiated dendrites were further loaded into fabrics, and the fabrics exhibited excellent antibacterial properties. Mask and towel fabricated with the antibacterial fabrics showed obviously reduced bacterial residue compared to their commercial counterparts. The reported molecular coordination method paves the way for the design of nature-inspired topological materials, and the obtained Zn_2GeO_4:Mn radiated dendrites have broad application prospects in the fields of industry and medical equipment.

2. Results and Discussion

2.1. Characterization of Zn_2GeO_4:Mn Radiated Dendrites

The topological Zn_2GeO_4:Mn radiated dendrites were prepared by the molecular coordination method. As shown in **Figure 1**a, uniform Zn_2GeO_4:Mn flower-like dendrites with dense and sharp spikes were obtained by using triethylenetetramine as the ligand. The mean size of the dendrites was about 7 μm (Figure S1, Supporting Information). Elemental mapping images and EDX analysis show the homogeneous distribution of Zn, Ge, O, and Mn in the Zn_2GeO_4:Mn dendrites (Figure 1b; Figure S2, Supporting Information). Nitrogen adsorption and desorption isotherms of Zn_2GeO_4:Mn dendrites exhibit a typical type-IV curve, indicating the presence of mesopores in the dendrites (Figure S3, Supporting Information).[2a] The porous structure of Zn_2GeO_4:Mn dendrites is favorable for the diffusion of active molecules including ROS within the dendrites. The dendrites possess a large Brunauer–Emmett–Teller surface area of 15.801 $m^2 \cdot g^{-1}$, which can afford rich active sites for surface adhesion and photocatalytic ROS generation. According to our previous studies, Zn_2GeO_4:Mn can store excitation energy in its intrinsic defects, and further produce persistent luminescence after the stoppage of excitation.[9b,10] The presence of defects was confirmed by the symmetric absorption peak detected in an electron paramagnetic resonance (EPR) assay (Figure S4, Supporting Information). Strong long-lifetime emission is detected in the Zn_2GeO_4:Mn dendrites (Figure 1c). The emission peak at 536 nm is ascribed to the characteristic $^4T_1$–$^6A_1$ transition of Mn^{2+}.[10a] The excitation spectrum of Zn_2GeO_4:Mn dendrites show a strong excitation band around 330 nm (Figure S5, Supporting Information). The luminescence images of Zn_2GeO_4:Mn dendrites before and after excitation ceases were collected with a commercial camera (Figure 1d). The Zn_2GeO_4:Mn dendrites exhibit intense green emission under the illumination, and strong persistent luminescence is observed after the removal of excitation (Figure 1d; Video S1, Supporting Information). The persistent luminescence of Zn_2GeO_4:Mn dendrites was further studied. The Zn_2GeO_4:Mn dendrites exhibit strong persistent luminescence and long decay time over 2 h (Figure 1e), which indicates the
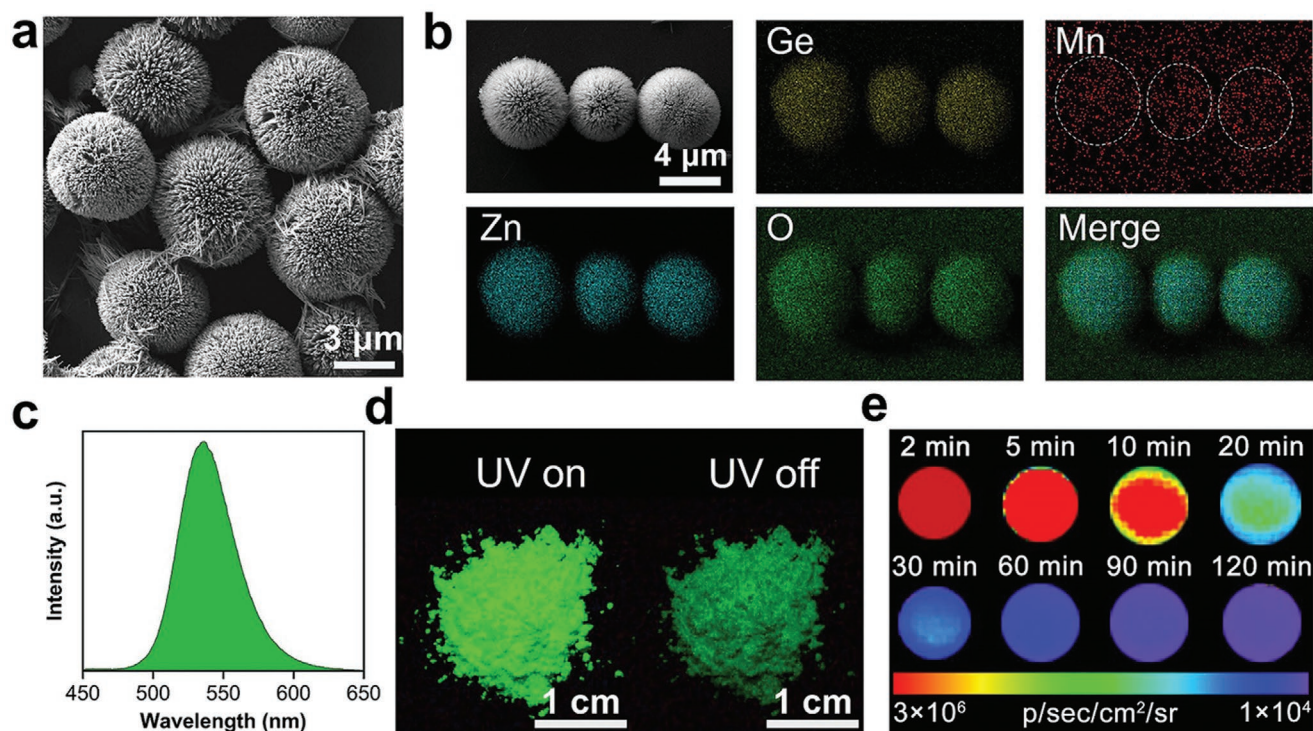

Figure 1. a) SEM image and b) elemental mapping images of the Zn_2GeO_4:Mn radiated dendrites. c) Phosphorescence spectrum of Zn_2GeO_4:Mn radiated dendrites. d) The luminescence images of Zn_2GeO_4:Mn radiated dendrites before and after excitation ceases. e) Images of the persistent luminescence decay of Zn_2GeO_4:Mn radiated dendrites.

**ADVANCED
SCIENCE NEWS**

www.advancedsciencenews.com

NANO · MICRO

small

www.small-journal.com

presence of a large number of defects in Zn_2GeO_4:Mn dendrites. The photoluminescence decay curve of the Zn_2GeO_4:Mn dendrites was presented in Figure S6, Supporting Information and the average photoluminescence lifetime is about 4.6 ms, indicating the presence of long-lived photo-excited electrons in the Zn_2GeO_4:Mn.The abundant defects in Zn_2GeO_4:Mn dendrites can efficiently store the excitation energy, and the stored energy can be slowly released to continuously produce ROS in the dark. Altogether, the prepared Zn_2GeO_4:Mn dendrites possess radiated topological structure, large surface area, and excellent photo-energy trapping capacity, which empowers the dendrites with great potential for high-affinity bio-adhesion and persistent photocatalysis.

2.2. The Regulation of the Topological Structure of Zn_2GeO_4:Mn

The topological structure of the Zn_2GeO_4:Mn can be easily regulated by changing the coordination capability of the amine ligand in the reaction system. **Figure 2**a shows that Zn_2GeO_4:Mn nanorods with irregular length and diameter are obtained when pure water is used as the solvent. The introduction of amine ligands with different coordination abilities including ethylenediamine, butanediamine, and diethylenetriamine produced a series of Zn_2GeO_4:Mn dumbbell-like spiky dendrites (Figure 2b–d; Figure S7, Supporting Information). It is noteworthy that the spikes in the Zn_2GeO_4:Mn dumbbell-like dendrites synthesized with different ligands show variable diameters, decreasing from 214.1 to 59.8 nm with the increased number of amino groups in the ligand (Figure S8, Supporting Information). When triethylenetetramine was used as the ligand, nearly spherical Zn_2GeO_4:Mn flower-like dendrites were obtained, and the diameter of spikes composing the dendrites was about 25 nm (Figure 2e; Figure S8, Supporting Information). With the increase of amino groups in the ligand, the morphology of Zn_2GeO_4:Mn changed from nanorod to dumbbell and finally to sphere, and at the same time, the diameter of the spikes composing the dendrites decreases gradually.
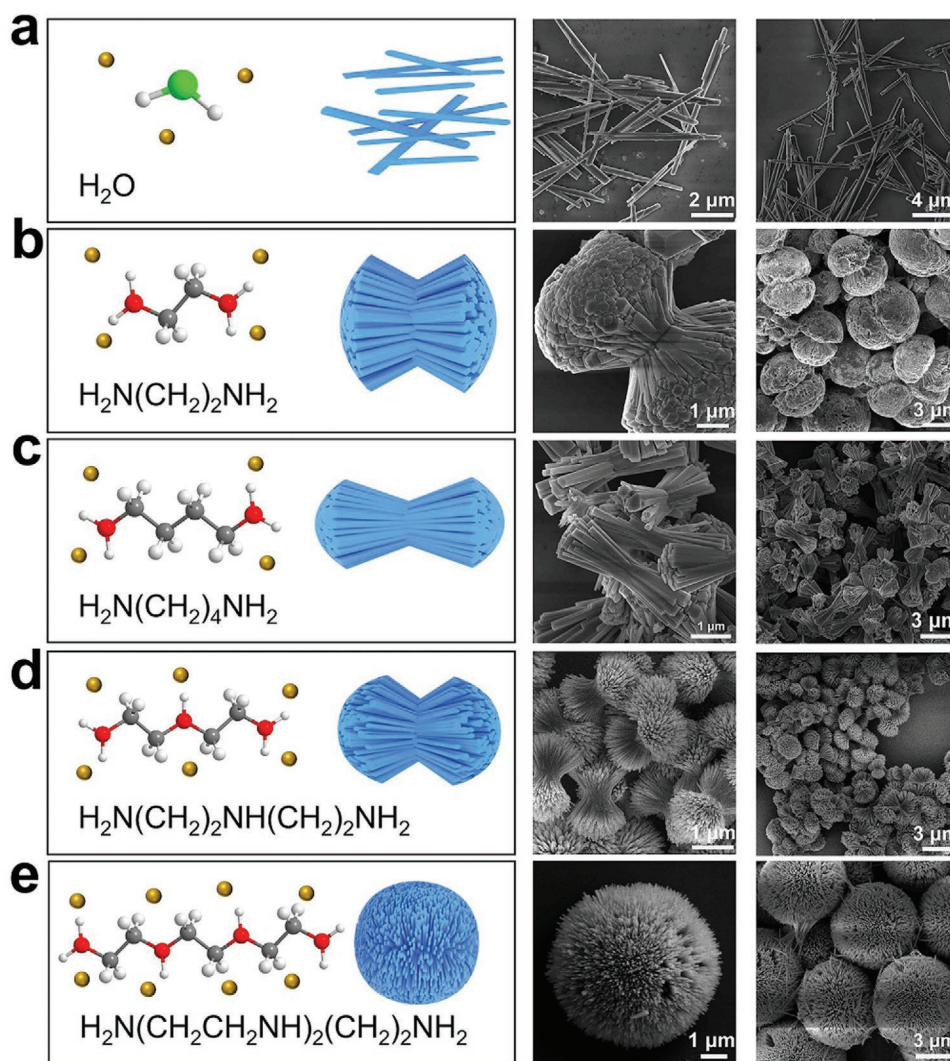
Figure 2. The structure of the used ligand, the schematic illustration, and SEM images of Zn_2GeO_4:Mn persistent phosphors synthesized with a) pure water, b) ethylenediamine/water, c) butanediamine/water, d) diethylenetriamine/water, and e) triethylenetetramine/water.

2100562 (3 of 9)

**ADVANCED
SCIENCE NEWS**
www.advancedsciencenews.com

NANO · MICRO
small
www.small-journal.com

Besides, the crystal structure and luminescence properties of Zn_2GeO_4:Mn are not affected by the coordination capability of the ligand (Figures S9 and S10, Supporting Information). These results imply that the topological structure of the Zn_2GeO_4:Mn persistent phosphors can be well-regulated by changing the coordination capability of the ligand in the reaction system.

The regulation of the topological structure of Zn_2GeO_4:Mn persistent phosphors is based on the solvent coordination molecular template mechanism.[11] During the solvothermal reaction, the organic amines can serve as a structure-directing reagent for the formation of topological Zn_2GeO_4:Mn persistent phosphors.[12] At the initial stage of the reaction, seed crystals are formed and aggregated orderly to generate the Zn_2GeO_4:Mn crystal nucleus.[12a,13] The -NH_2 groups of the organic amines selectively bind to specific crystallographic facets of the Zn_2GeO_4:Mn nucleus by coordinating with the surface metal ions.[14] The energy and growth rate of the amine-bound facets are reduced, whereas the growth of the unbound facets is not influenced.[4b] The many unbound facets serve as the nuclei sites for the growth of Zn_2GeO_4:Mn nanocrystals, which leads to the generation of the branched topological structure of Zn_2GeO_4:Mn dendrites over time. The morphology and diameter of the spikes composing the Zn_2GeO_4:Mn dendrites are also regulated by the organic amines. The (110) and (113) planes of the spikes are clearly observed in the HRTEM images of Zn_2GeO_4:Mn dendrites (Figure S11, Supporting Information). The lattice fringes of the (110) plane are parallel to the direction of spikes grows, and the (113) plane is at an angle of 66° with the spike direction. The HRTEM images reveal that the organic amines preferentially bind to the (110) plane to inhibit its growth, and the spikes grow along the (001) plane of Zn_2GeO_4:Mn phosphors to form the rod-like structure (Figures S12–S15, Supporting Information).[12a] Moreover, the multidentate ligands exhibit enhanced binding strength and coordination capability compared with bidentate ligands due to their multiple anchor atoms.[15] Thus the diethylenetriamine and triethylenetetramine with multiple anchor atoms show enhanced binding affinity to the (110) plane than ethylenediamine and butanediamine. That is, the inhibitory effect of diethylenetriamine and triethylenetetramine on the growth of the (110) plane was enhanced, thus the crystal grew along the (001) plane to form the spikes with a smaller diameter. The above analysis shows that the topological structure of Zn_2GeO_4:Mn persistent phosphors can be easily regulated by the molecular coordination method.
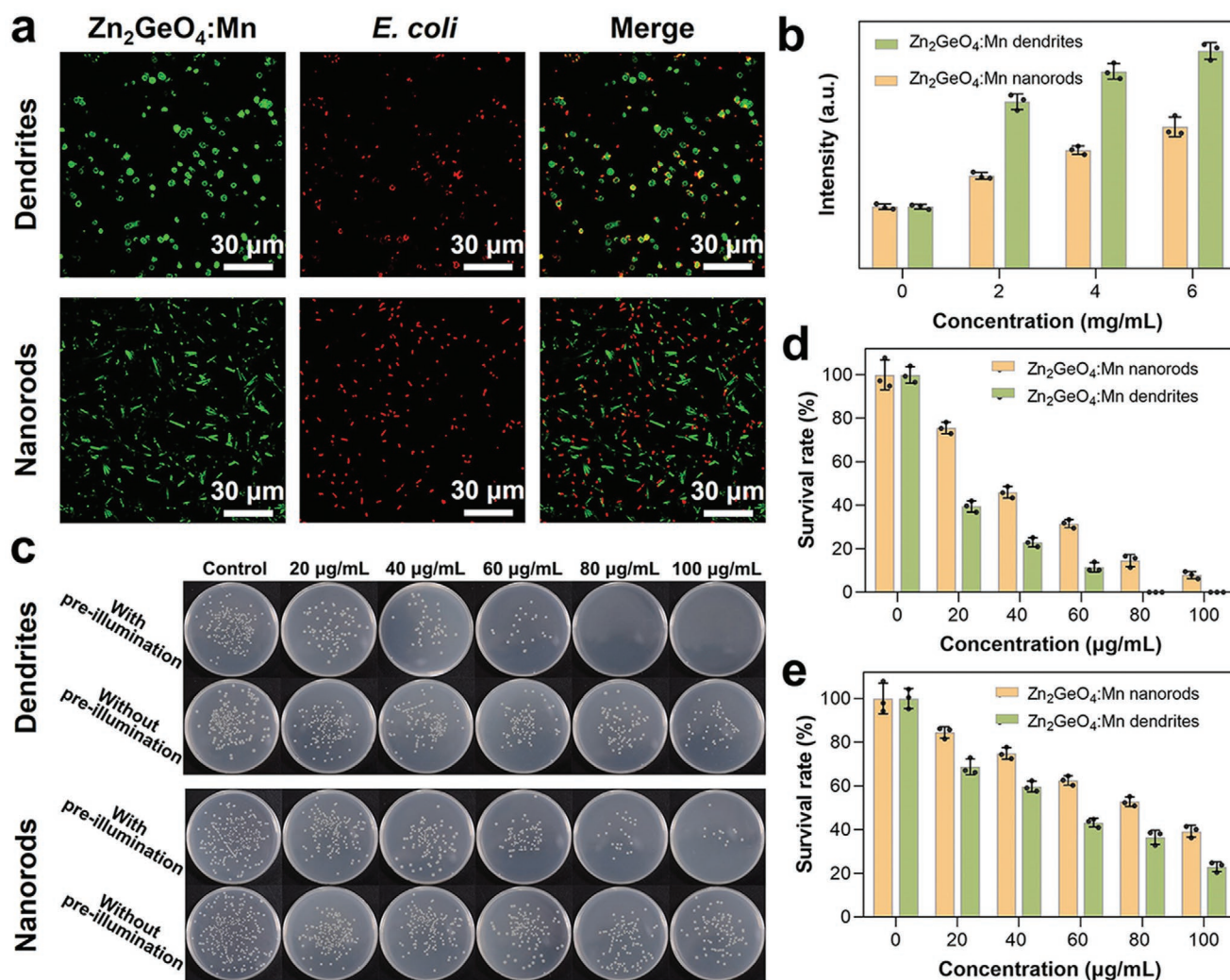
2.3. The Persistent Antibacterial Activity of Zn_2GeO_4:Mn Radiated Dendrites

Since radiated substances in nature show enhanced adhesion toward organisms, the radiated topological structure may also endow the Zn_2GeO_4:Mn dendrites with enhanced adhesion to bacteria or cells. In a proof of concept study, the adhesion properties of Zn_2GeO_4:Mn dendrites to bacteria were studied by taking *Escherichia coli* as a model, and the Zn_2GeO_4:Mn nanorods were used as a control (Figures S16–S18, Supporting Information). The materials-bacteria adhesion was directly observed with confocal fluorescence microscopy after incubating *E. coli* with the Zn_2GeO_4:Mn flower-like dendrites and

Zn_2GeO_4:Mn nanorods, respectively. As shown in **Figure 3**a and Figure S19, Supporting Information, most *E. coli* (red channel) were observed to adhere to the Zn_2GeO_4:Mn dendrites (green channel). Whereas the binding between nanorods and *E. coli* was significantly weaker than that of the dendrites and *E. coli*, indicating that the Zn_2GeO_4:Mn dendrites possess enhanced adhesion toward bacteria. The enhanced bacterial adhesion of Zn_2GeO_4:Mn dendrites can be ascribed to the structural matching and multivalent interactions between the spikes and the rough bacteria surface.

Furthermore, the LPPC activity of the Zn_2GeO_4:Mn was investigated by measuring the ROS produced in dark by the pre-illuminated Zn_2GeO_4:Mn. Figure 3b shows the concentration-dependent ROS production of the Zn_2GeO_4:Mn dendrites and Zn_2GeO_4:Mn nanorods in the dark by using 2′,7′-dichlorofluorescin (DCFH) as the fluorescence probe. Increased fluorescence intensity of 2′,7′-dichlorofluorescein (DCF) was detected when incubated DCFH with increased concentration of pre-illuminated Zn_2GeO_4:Mn dendrites or Zn_2GeO_4:Mn nanorods (Figure S20, Supporting Information), which confirms the LPPC activity of Zn_2GeO_4:Mn. Moreover, a higher amount of ROS production by Zn_2GeO_4:Mn dendrites is observed compared with Zn_2GeO_4:Mn nanorods, which can be ascribed to the higher specific surface area of Zn_2GeO_4:Mn dendrites in providing abundant active sites for ROS generation (Figure S3, Supporting Information). In addition, ROS production of Zn_2GeO_4:Mn also increases with the increase of pre-illumination time (Figure S21, Supporting Information). EPR was further carried out to investigate the ROS formation by the pre-illuminated Zn_2GeO_4:Mn dendrites, and 2,2,6,6-tetramethylpiperidine (TEMP) was used as a specific spin trapper. The characteristic EPR spectrum with three equally intense lines of 2,2,6,6-tetramethylpiperidine 1-oxyl (TEMPO) indicates the generation of singlet oxygen by the pre-illuminated Zn_2GeO_4:Mn dendrites (Figures S22 and S23, Supporting Information).[16] The EPR assay further confirms the good photocatalytic capability of the Zn_2GeO_4:Mn dendrites in the dark, suggesting the potential applications of Zn_2GeO_4:Mn dendrites in areas such as bacterial ablation and photodynamic therapy.

The good bacterial adhesion ability and LPPC activity encouraged us to explore the application of Zn_2GeO_4:Mn flower-like dendrites in persistent photocatalytic bacterial inactivation. The persistent antibacterial activity of pre-illuminated Zn_2GeO_4:Mn dendrites and Zn_2GeO_4:Mn nanorods was further examined. As shown in Figure 3c, reduced colony number is observed with the increased concentrations of pre-illuminated Zn_2GeO_4:Mn dendrites and nanorods, suggesting that the antibacterial effect of Zn_2GeO_4:Mn was concentration-dependent. Almost all of the bacteria were killed by pre-illuminated Zn_2GeO_4:Mn dendrites at the concentration of above 80 µg mL^{-1} in the dark. Whereas the bacterial inactivation percentage for pre-illuminated Zn_2GeO_4:Mn nanorods under the same concentrations was about 80%, much lower than that of Zn_2GeO_4:Mn dendrites (Figure 3d). The antibacterial performance of the pre-illuminated Zn_2GeO_4:Mn dendrites shows time-dependent feature, and almost all of the bacteria were killed after incubating the bacteria with the Zn_2GeO_4:Mn dendrites for 1.5 h (Figure S24, Supporting Information). Moreover,

ADVANCED
SCIENCE NEWS

www.advancedsciencenews.com

NANO · MICRO
small
www.small-journal.com

Figure 3. a) The confocal fluorescence images of *E. coli* adhered with Zn_2GeO_4:Mn dendrites and nanorods, green: Zn_2GeO_4:Mn; red: *E. coli*. b) ROS production of the pre-illuminated Zn_2GeO_4:Mn dendrites and Zn_2GeO_4:Mn nanorods with different concentrations in the dark. c) Photographs of colonies of *E. coli* after being incubated with 0, 20, 40, 60, 80, and 100 µg mL^{-1} Zn_2GeO_4:Mn dendrites and Zn_2GeO_4:Mn nanorods dispersion. The relative bacterial survival rate of *E. coli* after incubation with 0, 20, 40, 60, 80, and 100 µg mL^{-1} Zn_2GeO_4:Mn dendrites and Zn_2GeO_4:Mn nanorods dispersion d) with pre-illumination and e) without pre-illumination in the dark for 2 h.

we noticed that Zn_2GeO_4:Mn dendrites and Zn_2GeO_4:Mn nanorods can also kill bacteria partially even without pre-illumination (Figure 3e), which can be explained by the fact that the spikes on the surface of the dendrites and the sharp nanorods can act as a surgical knife to lancinate bacteria.[17] The better antibacterial performance of Zn_2GeO_4:Mn dendrites can be ascribed to the enhanced adhesion toward bacteria and better LPPC activity than nanorods. The antibacterial effect of pre-illuminated Zn_2GeO_4:Mn dendrites and nanorods toward Gram-positive bacteria *Staphylococcus aureus* was further investigated (Figure S25, Supporting Information), and good bacterial inhibition effect is observed, demonstrating the universal antibacterial capacity of the Zn_2GeO_4:Mn. Compared with traditional photocatalysts, the Zn_2GeO_4:Mn dendrites can not only kill bacteria under excitation but can also inhibit bacterial growth continuously after excitation ceases. The persistent antibacterial activity of Zn_2GeO_4:Mn dendrites in the dark can open

up new potentials such as continuous solar-powered bacterial inhibition during the daytime and at night. Collectively, the above results demonstrate that the Zn_2GeO_4:Mn dendrites with radiated topological structure and LPPC activity can adhere to and inactivate bacteria effectively, and the persistent antibacterial activity makes Zn_2GeO_4:Mn dendrites valuable in long-term environmental and medical protection.

2.4. The Antibacterial Mechanism of the Zn_2GeO_4:Mn Radiated Dendrites

To investigate the possible antibacterial mechanism of the Zn_2GeO_4:Mn dendrites, the bacterial structure and intracellular redox status of *E. coli* were further investigated. The morphological change of *E. coli* was visualized using SEM to investigate the effect of Zn_2GeO_4:Mn dendrites on bacteria. As shown
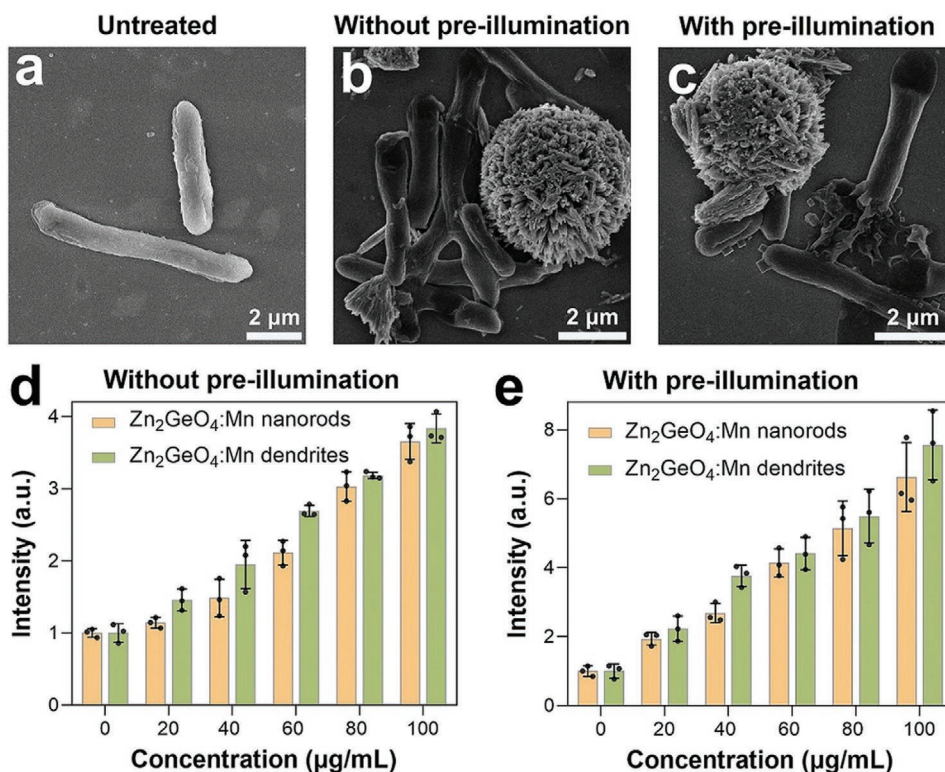
Figure 4. The SEM images of a) untreated *E. coli*, b) *E. coli* treated with Zn_2GeO_4:Mn dendrites without pre-illumination and c) with pre-illumination in the dark for 2 h, respectively. Intracellular ROS production of treated *E. coli* with 0, 20, 40, 60, 80, and 100 µg mL^{-1} Zn_2GeO_4:Mn dendrites and Zn_2GeO_4:Mn nanorods d) without pre-illumination and e) with pre-illumination in the dark for 2 h.

in **Figure 4**a, untreated *E. coli* is rod-shaped with an intact and smooth surface. Figure 4b shows that damaged cell walls with the holey surface can be clearly observed from *E. coli* treated with the un-illuminated Zn_2GeO_4:Mn dendrites. The damage of the cell wall by the Zn_2GeO_4:Mn dendrites can be ascribed to mechanical pressure from spikes.[17] As observed in Figure 4c, the morphology of *E. coli* is significantly changed after incubation with pre-illuminated Zn_2GeO_4:Mn dendrites. Obviously, the cell wall loses integrity and becomes partially wrinkled, and collapsed structures are also observed on the surface of *E. coli*. It is worth noting that the damage on *E. coli* caused by pre-illuminated Zn_2GeO_4:Mn dendrites is severe than that of the un-illuminated Zn_2GeO_4:Mn dendrites, indicating that the ROS generated by pre-illuminated Zn_2GeO_4:Mn dendrites can further aggravate the destruction of the cell wall. The morphological change shows the serious damage of bacteria cell wall by the Zn_2GeO_4:Mn dendrites, and such damage inevitably leads to bacterial death. Since the antibacterial effect of the Zn_2GeO_4:Mn dendrites is closely related to their ROS production, the total ROS produced in *E. coli* treated with Zn_2GeO_4:Mn dendrites was further examined by fluorescence assay. As shown in Figure 4d, increased fluorescence intensity is observed in *E. coli* exposed to un-illuminated Zn_2GeO_4:Mn dendrites and Zn_2GeO_4:Mn nanorods, which can be ascribed to the cell wall destruction of bacteria triggered by the sharp radiated spikes in Zn_2GeO_4:Mn dendrites and nanorods. Furtherly, the bacteria treated with pre-illuminated Zn_2GeO_4:Mn dendrites and Zn_2GeO_4:Mn nanorods produce more potent fluorescence

signal than that of the Zn_2GeO_4:Mn without pre-illumination (Figure 4e). The significantly increased ROS production in *E. coli* treated with pre-illuminated Zn_2GeO_4:Mn dendrites is well consistent with the results observed by SEM. These results suggest that intracellular ROS production in *E. coli* can be ascribed to the synergy effect of sharp spikes and singlet oxygen generation in Zn_2GeO_4:Mn dendrites, which can destroy the cell wall and cell organelles directly. Altogether, the above results indicate that the oxidative stress triggered by mechanical pressure and ROS are probably the reasons for bacterial inactivation by the Zn_2GeO_4:Mn dendrites.

2.5. The Antibacterial Properties of Zn_2GeO_4:Mn Dendrites-Coated Fabrics

The development of antibacterial fabrics has attracted increasing attention as bacteria in fabrics lead to serious problems to public health. Antibacterial fabrics could effectively kill the bacteria and reduce disease infections, and have played important roles in fields including hygiene, medicine, etc. Benefiting from their enhanced adhesion ability and intriguing antibacterial activity, we strive to develop antibacterial fabrics based on the Zn_2GeO_4:Mn flower-like dendrites (**Figure 5**a). The antibacterial fabrics were obtained by depositing Zn_2GeO_4:Mn dendrites on fabrics via a simple immersion method. As evidenced by SEM, Zn_2GeO_4:Mn dendrites are layered on the fibers of fabric uniformly, whereas the uncoated fabric looks
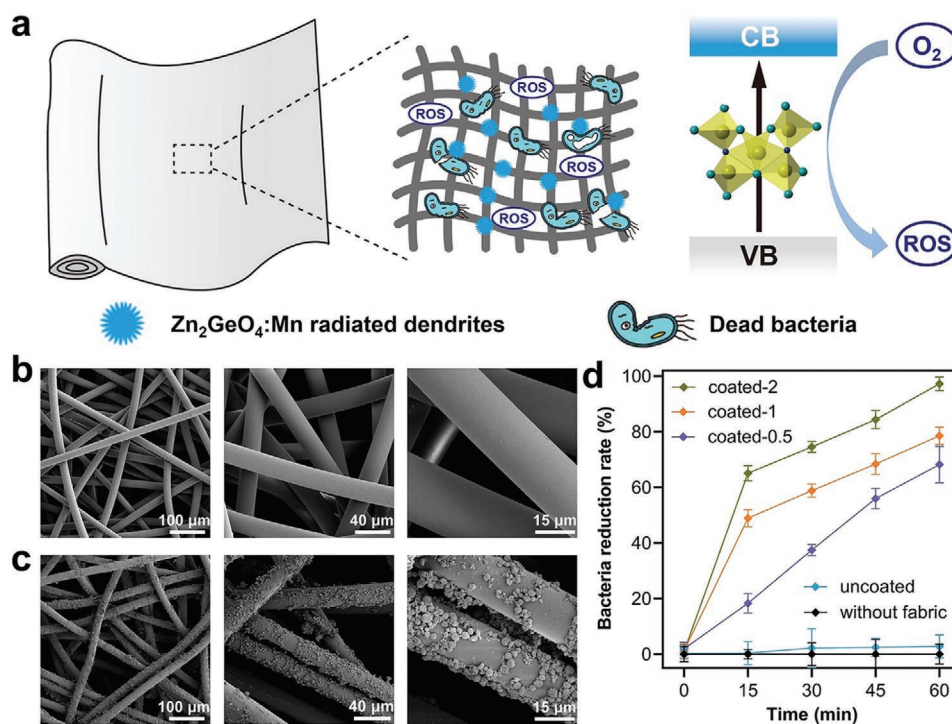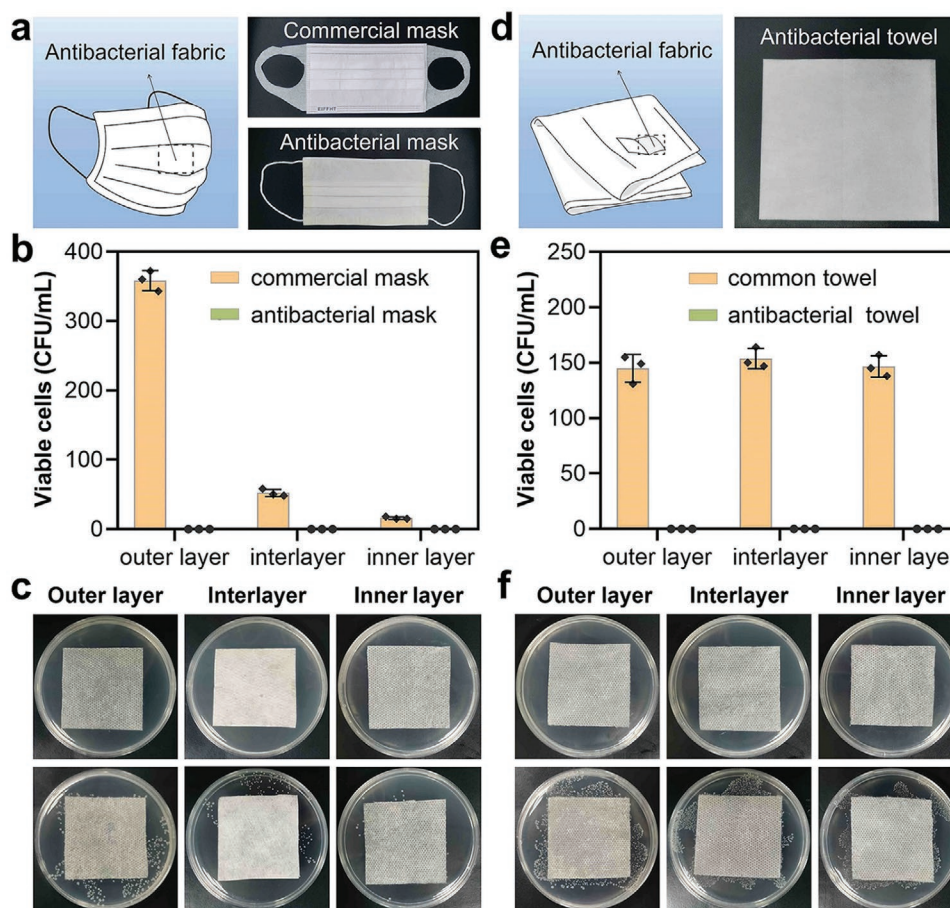
Figure 5. a) Schematic illustration of Zn_2GeO_4:Mn dendrites coated fabric for photocatalytic antibacterial applications. The SEM images of b) uncoated fabric and c) Zn_2GeO_4:Mn dendrites coated fabric. d) The bacterial reduction rate of fabrics coated with 0.5, 1, and 2 mg mL^{-1} Zn_2GeO_4:Mn dendrites, uncoated fabric, and without fabric.

smooth (Figure 5b,c; Figures S26 and S27, Supporting Information). The successful integration of Zn_2GeO_4:Mn dendrites into the fabric can be attributed to the enhanced adhesion affinity of radiated spikes toward fiber in fabric. The antibacterial activity of fabrics coated with 0.5, 1, and 2 mg mL^{-1} of Zn_2GeO_4:Mn dendrites (namely coated-0.5, coated-1, and coated-2) was evaluated by exposing the fabrics to *E. coli* suspension (Figure 5d). As anticipated, the Zn_2GeO_4:Mn dendrites-coated fabrics exhibit a significant decrease in the bacterial population, and the bacterial reduction rate of coated fabrics shows a close correlation with the illumination time and the concentration of coated Zn_2GeO_4:Mn dendrites, whereas the uncoated fabric shows no antibacterial activity. The excellent antibacterial activity of the developed fabrics can be ascribed to the good adhesion affinity and photocatalytic activity of the Zn_2GeO_4:Mn dendrites. When the antibacterial fabrics are exposed to bacteria, the dendrites in the fabrics can capture bacteria and further produce ROS for bacterial inactivation. These results confirm the successful fabrication and the potent antibacterial performance of the Zn_2GeO_4:Mn dendrites-based antibacterial fabrics.

2.6. The Zn_2GeO_4:Mn Dendrites Loaded Fabrics Used for Daily Personal Protection

The robust antibacterial performance of antibacterial fabrics encourages us to investigate the flexibility of the fabrics in various scenarios. As a proof of concept test, mask and towel were further fabricated by the antibacterial fabrics to verify the wide application potential of the antibacterial fabrics in daily

life. As shown in **Figure 6**a, the antibacterial fabric serves as the outer biocidal layer of antibacterial mask. The melt-blown fabric and uncoated-fabric are used as the interlayer and inner layer, respectively. The antibacterial capability of the obtained mask was studied by exposing the outer layer of the mask to *E. coli* aerosols. As shown in Figure 6b,c, the number of *E. coli* reduces significantly on each layer of antibacterial mask compared with that of the commercial mask after illumination. It is worth noting that no *E. coli* are observed on each layer of the antibacterial mask, whereas a small amount of *E. coli* is observed on the inner layer of the commercial mask. These results demonstrate that the antibacterial mask can efficiently inactive the bacteria before they migrate from the outer layer to the inner layer of the mask. Whereas, bacteria can still pass through the commercial mask and may further be inhaled into our bodies, posing threats to our health. Therefore, the developed antibacterial mask can provide much stronger guarantee in preventing bacterial infections than its commercial counterparts. It is also worth noting that the reutilization and extended life of the antibacterial mask can be realized due to its potent ability in bacterial inhibition (Figure S28, Supporting Information), which will be conducive to resource conservation and environmental protection. Likewise, antibacterial towel based on Zn_2GeO_4:Mn dendrites was obtained with an antibacterial interlayer sandwiched between two layers of uncoated-fabric (Figure 6d). The antibacterial ability of the towel was determined after soaking the towel in the bacterial suspension. The towel exhibited satisfactory antibacterial effect, and nearly all of the *E. coli* were killed (Figure 6e,f). In contrast, countless bacteria can be seen on the common

ADVANCED
SCIENCE NEWS
www.advancedsciencenews.com

NANO · MICRO
small
www.small-journal.com

Figure 6. a) The schematic illustration and optical images of Zn_2GeO_4:Mn dendrites-based antibacterial mask and commercial mask. b,c) Residual *E. coli* on the outer layer, interlayer, and inner layer of the antibacterial mask (top) and commercial mask (bottom). d) The schematic illustration and optical image of Zn_2GeO_4:Mn dendrites-based antibacterial towel. e,f) Residual *E. coli* on the outer layer, interlayer, and inner layer of the antibacterial towel (top) and common towel (bottom).

towel without Zn_2GeO_4:Mn dendrites coating. Taken together, the results suggest the feasibility and flexibility of antibacterial fabrics for infection prevention in practical application. Besides antibacterial masks and towels, the antibacterial fabrics are desirable to develop more multifunctional fabrics based protective and coating products.

3. Conclusion

In summary, a series of Zn_2GeO_4:Mn persistent phosphors with different surface topologies were prepared through a molecular coordination method. By changing the coordination capability of ligand used in the reaction system, the topological structure of the Zn_2GeO_4:Mn phosphors can be regulated from nanorods to radiated dendrites. Due to the radiated surface topologies mediated multivalent interactions and LPPC activity, Zn_2GeO_4:Mn radiated dendrites exhibit strong bacterial adhesion capacity and persistent photocatalytic antibacterial properties. Furthermore, Zn_2GeO_4:Mn dendrites coated fabrics were developed and displayed potent bacteria inactivation effect. The antibacterial mask and towel fabricated with Zn_2GeO_4:Mn dendrites coated fabrics displayed more efficient

bacterial inhibition ability compared to their commercial and common counterparts. Particularly, the developed antibacterial mask can effectively prevent the passage of bacteria, and provide a much stronger safety guarantee for us. The developed molecular coordination method provides a pathway for the rational design of nature-inspired functional materials with controllable surface topologies, and the obtained Zn_2GeO_4:Mn persistent radiated dendrites show great potential for applications in public health settings, packaging, and surgical equipment.

Supporting Information

Supporting Information is available from the Wiley Online Library or from the author.

Acknowledgements

Conflict of Interest

The authors declare no conflict of interest.

Data Availability Statement

Research data are not shared.

Keywords

bacterial inhibition, persistent luminescence, photocatalysis, topological structure

[1] a) T. Ni, S. Gerard, G. P. Zhao, K. Dent, J. Y. Ning, J. Zhou, J. Shi, J. Anderson-Daniels, W. Li, S. Jang, A. Engelman, C. Aiken, P. J. Zhang, *Nat. Struct. Mol. Biol.* **2020**, *27*, 855; b) T. Murakami, N. Carmona, A. Ono, *Proc. Natl. Acad. Sci. U. S. A.* **2020**, *117*, 8055; c) J. Wang, H.-J. Chen, T. Hang, Y. Yu, G. S. Liu, G. He, S. Xiao, B.-R. Yang, C. D. Yang, F. M. Liu, M. X. Wu, X. Xie, *Nat. Nanotechnol.* **2018**, *13*, 1078; d) S. Fujii, T. Tsuchimatsu, Y. Kimura, S. Ishida, S. Tangpranomkorn, H. Shimosato-Asano, M. Iwano, S. Furukawa, W. Itoyama, Y. Wada, K. K. Shimizu, S. Takayama, *Nat. Plants* **2019**, *5*, 731; e) R. Nathan, F. M. Schurr, O. Spiegel, O. Steinitz, A. Trakhtenbrot, A. Tsoar, *Trends Ecol. Evol.* **2008**, *23*, 638.

[2] a) H. Song, Y. A. Nor, M. H. Yu, Y. N. Yang, J. Zhang, H. W. Zhang, C. Xu, N. Mitter, C. Z. Yu, *J. Am. Chem. Soc.* **2016**, *138*, 6455; b) J. Zhang, G. Brown, J. Y. Fu, P. James, L. Mukandiwa, X. Huang, C. Z. Yu, *EcoMat* **2020**, *2*, e12028; c) T. C. Zhao, L. Chen, P. Y. Wang, B. H. Li, R. F. Lin, A. A. Al-Khalaf, W. N. Hozzein, F. Zhang, X. M. Li, D. Y. Zhao, *Nat. Commun.* **2019**, *10*, 4387.

[3] a) Y. T. Niu, M. H. Yu, S. B. Hartono, J. Yang, H. Y. Xu, H. W. Zhang, J. Zhang, J. Zou, A. Dexter, W. Y. Gu, C. Z. Yu, *Adv. Mater.* **2013**, *25*, 6233; b) W. X. Wang, P. Y. Wang, X. T. Tang, A. A. Elzatahry, S. W. Wang, D. Al-Dahyan, M. Y. Zhao, C. Yao, C.-T. Hung, X. H. Zhu, T. C. Zhao, X. M. Li, F. Zhang, D. Y. Zhao, *ACS Cent. Sci.* **2017**, *3*, 839.

[4] a) Y. Wang, Z. Z. Zhang, L. N. Zhang, Z. B. Luo, J. N. Shen, H. X. Lin, J. J. Long, J. C. Wu, X. Z. Fu, X. X. Wang, C. Li, *J. Am. Chem. Soc.* **2018**, *140*, 14595; b) E. Ye, M. D. Regulacio, S.-Y. Zhang, X. J. Loh, M.-Y. Han, *Chem. Soc. Rev.* **2015**, *44*, 6001; c) N. Liu, Z. D. Lu, J. Zhao, M. T. McDowell, H.-W. Lee, W. T. Zhao, Y. Cui, *Nat. Nanotechnol.* **2014**, *9*, 187; d) Z. Z. Wang, Y. Zhang, E. Ju, Z. Liu, F. F. Cao, Z. W. Chen, J. S. Ren, X. G. Qu, *Nat. Commun.* **2018**, *9*, 3334; e) X. L. Hu, J. M. Hu, J. Tian, Z. S. Ge, G. Y. Zhang, K. F. Luo, S. Y. Liu, *J. Am. Chem. Soc.* **2013**, *135*, 17617.

[5] a) V. Goriainov, R. Cook, J. M. Latham, D. G. Dunlop, R. O. C. Oreffo, *Acta Biomater.* **2014**, *10*, 4043; b) R. Chu, D. Yang, X. Meng, S. Yu, Y. Wan, J. Wu, J. Wang, *Front. Chem.* **2019**, *7*, 636; c) Z. Sun, A. Mehmani, C. Torres-Verdín, *Water Resour. Res.* **2021**, *57*, e2020WR028324; d) C. Buten, L. Kortekaas, B. J. Ravoo, *Adv. Mater.* **2020**, *32*, 1904957.

[6] a) K. Rechendorff, M. B. Hovgaard, M. Foss, V. P. Zhdanov, F. Besenbacher, *Langmuir* **2006**, *22*, 10885; b) P. Roach, D. Farrar, C. C. Perry, *J. Am. Chem. Soc.* **2006**, *128*, 3939; c) S. B. Yeldell, O. Seitz, *Chem. Soc. Rev.* **2020**, *49*, 6848; d) S. Tommasone, F. Allabush, Y. K. Tagger, J. Norman, M. Köpf, J. H. Tucker, P. M. Mendes, *Chem. Soc. Rev.* **2019**, *48*, 5488.

[7] a) C.-Y. Chiu, L. Y. Ruan, Y. Huang, *Chem. Soc. Rev.* **2013**, *42*, 2512; b) Z. H. Wu, S. L. Yang, W. Wu, *Nanoscale* **2016**, *8*, 1237; c) M. S. Jin, G. N. He, H. Zhang, J. Zeng, Z. X. Xie, Y. N. Xia, *Angew. Chem., Int. Ed.* **2011**, *50*, 10560.

[8] a) L. Xu, G. L. Wang, X. S. Zheng, H. B. Pan, J. F. Zhu, Z. Y. Li, S.-H. Yu, *Chem* **2018**, *4*, 2451; b) G. Wang, Y. Liu, C. Gao, L. Guo, M. Chi, K. Ijiro, M. Maeda, Y. Yin, *Chem* **2017**, *3*, 678; c) D. M. Liu, X. X. Xu, Y. Du, X. Qin, Y. H. Zhang, C. S. Ma, S. H. Wen, W. Ren, E. M. Goldys, J. A. Piper, S. X. Dou, X. G. Liu, D. Y. Jin, *Nat. Commun.* **2016**, *7*, 10254; d) X. H. Xia, J. Zeng, L. K. Oetjen, Q. G. Li, Y. N. Xia, *J. Am. Chem. Soc.* **2012**, *134*, 1793; e) Y. N. Xia, Y. J. Xiong, B. Lim, S. E. Skrabalak, *Angew. Chem., Int. Ed.* **2009**, *48*, 60.

[9] a) Q. Liu, Y. Zhou, J. H. Kou, X. Y. Chen, Z. P. Tian, J. Gao, S. C. Yan, Z. G. Zou, *J. Am. Chem. Soc.* **2010**, *132*, 14385; b) J. Wang, Q. Q. Ma, W. Zheng, H. Y. Liu, C. Q. Yin, F. B. Wang, X. Y. Chen, Q. Yuan, W. H. Tan, *ACS Nano* **2017**, *11*, 8185.

[10] a) Z. H. Li, Q. Wang, Q. Q. Ma, J. Wang, Z. H. Li, Y. X. Li, X. B. Lv, W. Wei, L. Chen, Q. Yuan, *Nano Res.* **2018**, *11*, 6167; b) J. Wang, Q. Q. Ma, H. Y. Liu, Y. Q. Wang, H. J. Shen, X. X. Hu, C. Ma, Q. Yuan, W. H. Tan, *Anal. Chem.* **2017**, *89*, 12764; c) H. Y. Liu, X. X. Hu, J. Wang, M. Liu, W. Wei, Q. Yuan, *Chin. Chem. Lett.* **2018**, *29*, 1641; d) J. Wang, Q. Q. Ma, Y. Q. Wang, H. J. Shen, Q. Yuan, *Nanoscale* **2017**, *9*, 6204.

[11] a) S. Kumar, T. Nann, *Small* **2006**, *2*, 316; b) Q. Liu, Y. Zhou, Z. P. Tian, X. Y. Chen, J. Gao, Z. G. Zou, *J. Mater. Chem.* **2012**, *22*, 2033.

[12] a) J. Liang, J. Xu, Q. Gu, Y. G. Zhou, C. C. Huang, H. X. Lin, X. X. Wang, *J. Mater. Chem. A* **2013**, *1*, 7798; b) H.-B. Yao, M.-R. Gao, S.-H. Yu, *Nanoscale* **2010**, *2*, 322.

[13] Z. B. Zhuang, X. T. Lu, Q. Peng, Y. D. Li, *J. Am. Chem. Soc.* **2010**, *132*, 1819.

[14] Y. C. Zhu, T. Mei, Y. Wang, Y. T. Qian, *J. Mater. Chem.* **2011**, *21*, 11457.

[15] a) X. Y. Xie, C. S. Cao, W. B. Wei, S. H. Zhou, X.-T. Wu, Q.-L. Zhu, *Nanoscale* **2020**, *12*, 5817; b) H. Zhang, Y. Z. Wu, C. Shen, E. Li, C. X. Yan, W. W. Zhang, H. Tian, L. Y. Han, W. H. Zhu, *Adv. Energy Mater.* **2019**, *9*, 1803573.

[16] C. Mendoza, A. Désert, L. Khrouz, C. A. Páez, S. Parola, B. Heinrichs, *Environ. Sci. Pollut. Res.* **2019**, https://doi.org/10.1007/s11356-019-04763-5.

[17] Q. Cai, Y. Y. Gao, T. Y. Gao, S. Lan, O. Simalou, X. Y. Zhou, Y. L. Zhang, C. Harnoode, G. Gao, A. Dong, *ACS Appl. Mater. Interfaces* **2016**, *8*, 10109.